Strong Mutual Coupling Effects on LOFAR: Modeling and In-Situ Validation

G. Virone, *Member, IEEE*, P. Bolli, F. Paonessa, G. Pupillo, S.J. Wijnholds, *Senior Member, IEEE*, S. Matteoli, *Senior Member, IEEE*, A. M. Lingua, J. Monari, G. Addamo, O. A. Peverini, *Member, IEEE*

***Abstract*— Front-end amplifiers with high input impedance are exploited to build active array elements for modern low-frequency radio telescopes. The combination of such loading and mutual coupling between adjacent elements is responsible for the deep nulls that are present in some Embedded Element Patterns (EEPs) of the Low Frequency Array (LOFAR). This paper quantifies this phenomenon with both models and experimental data. The full-wave array simulations and the measured amplifier scattering parameters are combined to obtain the EEP models. These models are in good agreement with the in-situ measurements that have been performed with a micro Unmanned Aerial Vehicle (UAV) carrying a field source.**

***Index Terms*—Antenna Arrays, Antenna Measurements, Antenna Radiation Patterns, Low-noise amplifiers, Mutual Coupling, Phased Arrays, Radio Astronomy, Unmanned Aerial Vehicles**

I. Introduction

TECHNOLOGICAL advances in antenna, RF and computer engineering have enabled the radio astronomical community to develop ground-breaking instruments for observations below 300 MHz using digital phased array technology. These developments have led to the Low Frequency Array (LOFAR) in Europe operating between 10 and 240 MHz [1] and the Murchison Widefield Array (MWA) in Australia operating in the 80 - 300 MHz range [2]. These instruments are considered technological pathfinder and precursor, respectively, for the Low Frequency Aperture Array (LFAA) system envisaged to operate in the 50 - 350 MHz range as part of the Square Kilometer Array (SKA) [3].

Manuscript submitted on October 10, 2017, revised December 26, 2017; accepted February 14, 2018.
This work was supported by the National Institute for Astrophysics under the TECNO INAF 2014 program and by the Netherlands Organization for Scientific Research.
G. Virone, F. Paonessa, S. Matteoli, G. Addamo and O. A. Peverini are with the Consiglio Nazionale delle Ricerche – Istituto di Elettronica e di Ingegneria dell'Informazione e delle Telecomunicazioni (CNR-IEIIT), Corso Duca degli Abruzzi 24, 10129, Turin, Italy (e-mail: giuseppe.virone@ieiit.cnr.it).
P.Bolli is with the Istituto Nazionale di AstroFisica - Osservatorio Astrofisico di Arcetri, Florence, Italy (e-mail: pbolli@arcetri.inaf.it)
G.Pupillo and J. Monari are with Istituto Nazionale di AstroFisica - Istituto di Radioastronomia, Bologna, Italy (e-mail: g.pupillo@ira.inaf.it).
S. J. Wijnholds is with the Netherlands Institute for Radio Astronomy (ASTRON), Dwingeloo, The Netherlands (e-mail: wijnholds@astron.nl).
A. M. Lingua is with the Environment, Land and Infrastructure Department (DIATI) – Politecnico di Torino, Corso Duca degli Abruzzi 24, 10128, Turin, Italy (e-mail: andrea.lingua@polito.it).

Fig. 1. Aerial view of the Low-Band Antennas (LBAs) of one LOFAR station.

An accurate electromagnetic description of such instruments in terms of experimentally-validated models is crucial in both design and operating stages. Both the LOFAR Low-band Antenna (LBA) array (a single station is visible in Fig. 1) and the LFAA stations (subarrays) have a random element distribution. Therefore, the knowledge of all Embedded Element Patterns (EEPs) is required to perform all trade-offs between performance, size and cost as well as to calibrate the digital beam forming system [4], [5].

The determination of a reliable and complete EEP look-up table is a very challenging task owing to the large size of the arrays (40 to 80 m), the interaction between the elements, their finite ground mesh over soil and the impedance mismatch of the front-end amplifiers. The latter is very significant in the LOFAR LBAs where a voltage-amplifier configuration (very high input impedance) is adopted as active element [6]. This cost-effective design solution was basically driven by the galactic-noise-dominated operating condition. Roughly speaking, the sky is very bright below 100 MHz, hence, the antenna noise temperature is so high that a matched low-noise front-end is not necessary to optimize the overall signal-to-noise ratio. On the other hand, it should be recalled that the EEP of an array element depends on the termination of all the other elements [7]. The reflected contributions arising at all the mismatched amplifier inputs are mutually coupled to the adjacent elements. This can in turn potentially produce significantly distorted EEPs rather than the desirable smooth dipole-like behavior.

This phenomenon is thoroughly quantified in this paper by means of the scattering-matrix formulation described in

section II. The model is compared to experimental results in section III. The latter were collected on a LOFAR station using of a UAV-mounted test source.

II. Modeling of the EEPs

A. Formulation

Full-wave electromagnetic analysis tools allow for the direct computation of the EEPs according to a predefined loading condition Z_L on the adjacent elements (e.g. lumped elements in FEKO [8]). Such an impedance can be directly used to model the effect of the amplifier input mismatch. Nevertheless, the following formulation has been derived in order to provide more physical insight on such a mismatch effect and to allow for efficient parametrical analyses with respect to the amplifier reflection coefficient values.

The whole system is described with the multi-port circuit in Fig. 2. The antenna array is described with its scattering matrix $\boldsymbol{S}$ having Z_0 as reference impedance. The radiated electric field $\boldsymbol{E}$ from the array (terminated on Z_0) in the far-field region can be expressed as

$$\boldsymbol{E}= \frac{e^{-jkR}}{R} \sum_{n=1}^{N} \boldsymbol{E}_n^{FF} (1 + \mathrm{S}_{nn}) \sqrt{Z_0}\, a_n \tag{1}$$

where the dependence on the observation angle is understood, k is the free-space propagation constant, R is the distance from the reference center (array center), N is the number of elements, S_{nn} are the diagonal elements of the NxN scattering matrix $\boldsymbol{S}$ i.e. the reflection coefficient of the n-th elements when all the other ports are loaded with Z_0 and a_n are the incident power waves (see Fig. 2, b_n are the scattered power waves). It should be noted that the term $(1 + \mathrm{S}_{nn})\sqrt{Z_0} a_n$ is equal to the total voltage at the n-th port. Finally, the $\boldsymbol{E}_n^{FF}$ are the E-field EEPs computed with an applied unitary voltage and with the coupled ports loaded on the reference impedance Z_0. For convenience, the $\boldsymbol{E}_n^{FF}$ will be hereafter referred to as the Z_0EEPs.

The EEPs in the Z_L-loaded condition ($Z_L \neq Z_0$) will be instead hereafter called Z_LEEPs. By definition, the Z_LEEP evaluation for the i-th element (whose input impedance is represented as Z_L in Fig. 2) is performed exciting only that particular element i.e. $a_i = 1\,\mathrm{W}^{1/2}$. Such an excitation produces the scattered power waves b_n toward the amplifiers owing to the mutual coupling (for $n \neq i$). The presence of the amplifiers input impedance $Z_L \neq Z_0$ in turn causes part of the energy to reflect back to the array. In this case, it is convenient to introduce the $N-1$ vector $\boldsymbol{a}^{(c)}$ containing the power waves a_n for all the elements having $n \neq i$ (i.e. the coupled elements). In particular, if Z_L=Z_0, then $\boldsymbol{a}^{(c)}$ is zero since there is no reflection from the amplifiers. Otherwise, after solving the circuit in Fig. 2, the $\boldsymbol{a}^{(c)}$ should be computed as

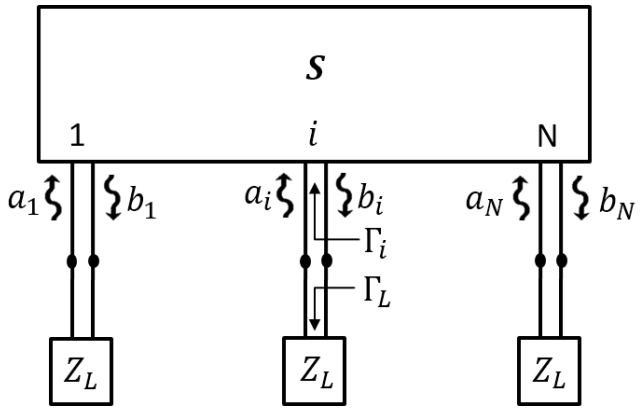

Fig. 2. Multi-port circuit: the array is represented with the scattering matrix $\boldsymbol{S}$, whereas Z_L is the amplifier impedance.

$$\boldsymbol{a}^{(c)} = \boldsymbol{\Gamma}_L \left(\boldsymbol{I} - \boldsymbol{S}^{(r)} \boldsymbol{\Gamma}_L\right)^{-1} \boldsymbol{S}^{(c)} a_i \tag{2}$$

where $\boldsymbol{\Gamma}_L$ is a diagonal matrix with size $N-1$ containing the amplifier reflection coefficients, $\boldsymbol{I}$ is the identity matrix, $\boldsymbol{S}^{(r)}$ is a $(N-1)$x$(N-1)$ submatrix containing $S_{nm}^{(r)} = S_{nm}$ with $n, m \neq i$ (i.e. the reflection and mutual coupling coefficients for the surrounding elements) and $\boldsymbol{S}^{(c)}$ is a N-1 column vector defined as $S_{ni}^{(c)} = S_{ni}$ with $n \neq i$, containing the mutual coupling coefficients from the i-th element to the surrounding n-th elements. The definition of $\boldsymbol{S}^{(c)}$ and $\boldsymbol{S}^{(r)}$ arise from proper arrangement of the array scattering matrix that is convenient for the cascade operations

$$\boldsymbol{S} = \begin{bmatrix} S_{ii} & \boldsymbol{S}^{(c)T} \\ \boldsymbol{S}^{(c)} & \boldsymbol{S}^{(r)} \end{bmatrix}.$$

The reflection coefficient Γ_i (see Fig. 2) at the i-th port is instead computed as

$$\Gamma_i = S_{ii} + \boldsymbol{S}^{(c)T} \boldsymbol{\Gamma}_L \left(\boldsymbol{I} - \boldsymbol{S}^{(r)} \boldsymbol{\Gamma}_L\right)^{-1} \boldsymbol{S}^{(c)} \tag{3}$$

Both (2) and (3) contain the term $\left(\boldsymbol{I} - \boldsymbol{S}^{(r)} \boldsymbol{\Gamma}_L\right)^{-1}$. It should be pointed out that this term can become large when $\boldsymbol{S}^{(r)} \boldsymbol{\Gamma}_L$ approaches the identity matrix. Such a resonance condition can occur when both the elements and the amplifier are mismatched with respect to the reference impedance and their phases are complementary with respect to 2π. It is apparent that at the resonance frequency the incident power waves $\boldsymbol{a}^{(c)}$ can become larger than $\boldsymbol{\Gamma}_L \boldsymbol{S}^{(c)} a_i$. This phenomenon can be seen as a magnification of the mutual coupling effect. As far as Γ_i is concerned, the resonant term on the right side of (3) is summed with S_{ii}. The resulting reflection level $|\Gamma_i|$ could thus be either higher or lower than $|S_{ii}|$.

The Gain pattern G_i for the i-th element is finally computed from (1)-(3) as

$$G_i = 4\pi \frac{Z_0}{Z} \frac{\left|\boldsymbol{E}_i^{FF}(1+\mathrm{S}_{ii})a_i + \sum_{k=1}^{N-1} \boldsymbol{E}_k^{(c)} a_k^{(c)}\right|^2}{(1-|\Gamma_i|^2)|a_i|^2} \tag{4}$$

where Z is the free-space impedance and the $\boldsymbol{E}_k^{(c)}$ are defined as $\boldsymbol{E}_n^{FF}(1+S_{nn})$ with $n \neq i$. As a result, the EEP in the Z_L-loaded condition (Z_LEEP) is described as a series of all the EEPs obtained in the Z_0-loaded condition (Z_0EEPs). It should be noted that, apart from the first term, the weights of such a linear combination are the elements of $\boldsymbol{a}^{(c)}$. Therefore, according to the considerations discussed above, the effect of the adjacent elements on the Z_LEEP is of course higher in highly mismatched conditions ($Z_L \neq Z_0$), where resonance phenomena can occur (2). In these conditions, the adjacent elements can be considered as parasitic elements (scatterers) that strongly modify the pattern of excited one [9]. This phenomenon has been deeply exploited in the literature to design a few classes of antennas, see for example the reactive controlled directive arrays [10], the bull's eye feeder [11], the EBG-enhanced structures [12],[13] and the holographic-inspired antenna [14]. This paper highlights the importance of the antenna-amplifier resonance in the framework of low-frequency aperture arrays for radio astronomy.

The same considerations can be derived from the impedance matrix formulation [10],[15]. In this case, the resonance term is represented by $(\boldsymbol{Z}_A + \mathrm{Z}_L\boldsymbol{I})^{-1}$, where $\boldsymbol{Z}_A$ is the array impedance matrix (open circuit loading). This term is proportional to the induced currents on the array elements that are maximum at resonance, yielding their maximum scattering effect.

B. Simulated Behavior

A LOFAR LBA station is composed of 96 dual-polarized inverted-V dipoles [6]. Each dipole is mounted on a 3 x 3 m^2 ground plane visible in both Fig. 1 and 3. Detailed FEKO models have been built for both the single antenna and the array [16] using a 50-Ω reference impedance (Z_0). The reflection coefficient magnitude of the single antenna Γ_A in Fig. 4a) (solid blue line) shows a resonance condition at 50 MHz. The front-end amplifier instead exhibits a reflection level Γ_L above -0.5 dB (dashed green line) across the whole frequency band. In Fig.4b), the phase of Γ_A (solid blue) exhibits a sharp variation across the antenna resonance whereas the phase of the amplifier Γ_L (dashed green) is more constant and below 0°, owing to its high and slightly capacitive impedance (voltage amplifier). The phase of the product $\Gamma_A\Gamma_L$ is also shown in Fig. 4b) with the dash-dotted red line. This quantity approaches 0° around 57 MHz (see vertical grey line). As a consequence, the magnitude of the quantity $1-\Gamma_A\Gamma_L$ in Fig. 4c) shows a minimum at the same frequency. It should be pointed out that the reflection coefficient of the isolated antenna Γ_A is a good approximation of the average element reflection coefficient in the sparse random array environment where the mutual coupling levels are low [17]. Hence, the quantity $1-\Gamma_A\Gamma_L$ can be considered as a good estimate of the diagonal elements of $\boldsymbol{I}-\boldsymbol{S}^{(r)}\boldsymbol{\Gamma}_L$ (see section II.A). For these reasons, the frequency of 57 MHz has been selected to investigate the resonance phenomena on the LBA.

Fig. 3. The UAV-mounted field source flying on the LBA inverted-V dipoles

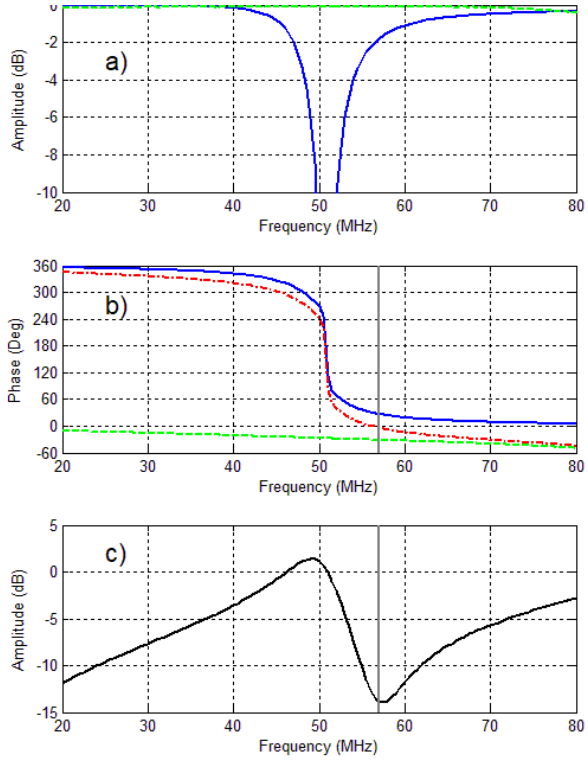

Fig. 4. a) Magnitude and b) phase of the reflection coefficients of a single LBA Γ_A (solid blue) and of the front-end amplifier Γ_L (dashed green). The reference impedance is 50 Ω. The phase of the product $\Gamma_A\Gamma_L$ is shown with the dash-dotted red line. The vertical grey line highlights the zero-crossing of $\angle\Gamma_A\Gamma_L$. c) Magnitude of the quantity $1-\Gamma_A\Gamma_L$ showing a minimum near 57 MHz.

It should be pointed out that the same resonance condition also appears in the transfer function of the active element (assembly of antenna and amplifier). Therefore, the consideration reported above also explains the frequency-shifted peak response of the LBA sensitivity in [18], which appears at 57 MHz instead of 50 MHz.

The random distribution of the inner elements of a LOFAR LBA station is shown in Fig. 5. It can be observed that the spacing is smaller for the elements that are closer to the center.

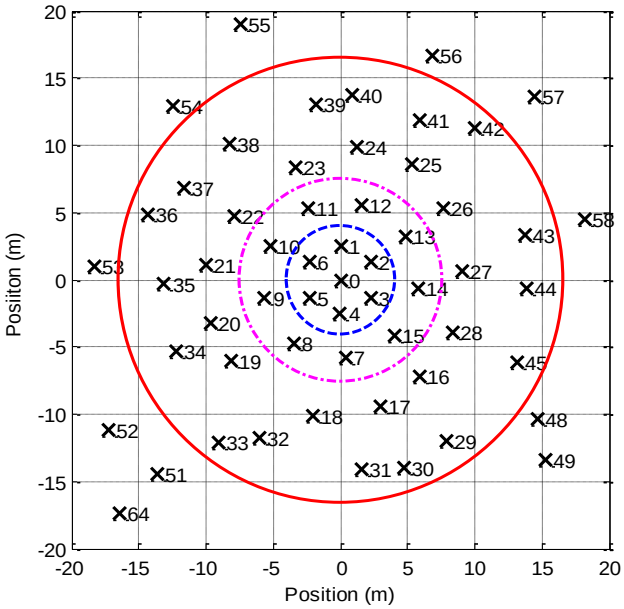

Fig. 5. Distribution of the inner elements of a LOFAR LBA station. The dashed-blue, dash-dotted magenta and the solid red circles identify those elements for which $\boldsymbol{a}^{(c)}/a_0$ (central one excited) is higher than -15 dB, -25 dB and -35 dB, respectively, at 57 MHz.

Such a distribution was conceived in order to improve the high-frequency performance [6]. A minimum element-distance requirement however yielded a quasi-regular distribution for elements 0-15. In this central region, the mutual-coupling mitigation effects of a random configuration [17] are basically not present. As a matter of fact, the computation of the Z_{L}EEP will be presented for the central element (#0) because it represents the worst case in terms of mutual coupling and pattern distortion.

The scattering matrix of the whole LBA array has been computed with FEKO. The products between the mutual coupling coefficients (central element excited) and the amplifier reflection coefficient ($\boldsymbol{\Gamma}_L\boldsymbol{S}^{(c)}$) are shown in Fig. 6. Solid black and dashed blue lines (both with dot markers) refer to the co- and cross-oriented dipoles, respectively. These curves represent the amount of power that is reflected at the amplifier input port if the interaction between the antenna and the amplifier (i.e. the term $\left(\boldsymbol{I}-\boldsymbol{S}^{(r)}\boldsymbol{\Gamma}_L\right)^{-1}$) is neglected. The abscissa of Fig. 6 is the element number, which is related to its distance from the array center (see Fig. 5). The first (closer) co-oriented dipoles exhibit an excitation level of about -25 dB, which is generally considered as non-critical. The other elements are below -35 dB. The solid red and dashed magenta curves (both with dot markers) instead show the excitation coefficients $\boldsymbol{a}^{(c)}/a_0$ computed with (2) for the co- and cross-oriented dipoles, respectively. It is apparent that the resonance phenomenon discussed above produces a significant enhancement of the excitation levels which are now higher than -15 dB for the closer elements (10 dB higher with respect to the black-curve) and higher than -35 dB for all the co-oriented elements up to number 48. It should be noted that the more remote elements exhibit a magnification effect that is even larger (20 dB) than the closer ones. A magnification

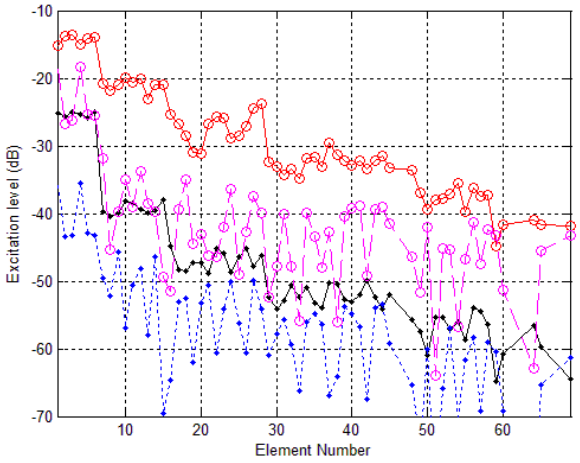

Fig. 6. Magnitude of the quantities $\boldsymbol{\Gamma}_L\boldsymbol{S}^{(c)}$ (co-oriented elements: black solid curve with dot markers, cross-oriented elements: blue dashed line with dot markers) and $\boldsymbol{a}^{(c)}/a_0$ (co-oriented elements: red solid curve with circle markers, cross-oriented elements: magenta dashed line with circle markers) for the LBA elements at 57 MHz with the central element (#0) excited.

effect of 20 dB is also visible for the closer cross-oriented dipoles (see dashed magenta with respect to dashed blue curve).

Fig. 7 shows the Z_{L}EEP for the central element of the LBA array at 57 MHz. It has been computed from (4) exploiting an increasing number of Z_L-loaded elements to investigate the convergence of such a series. The dotted black curve represents the Z_0EEP. As expected, it is close to a dipole-over-ground-plane because no significant resonance occurs in this case. The dashed blue curves instead represent the Z_{L}EEP computed by loading (with the amplifiers) the closer 6 co-oriented dipoles (dashed blue circle in Fig. 5), which are about 3 m away from the center ($\left|\boldsymbol{a}^{(c)}/a_0\right|$>-15 dB, see Fig. 6). It can be observed that these curves are completely different from the Z_0EEP. The dash-dotted magenta curves were obtained with 15 loaded elements (about 6m from the center, dash-dotted magenta circle in Fig. 5, $\left|\boldsymbol{a}^{(c)}/a_0\right|$>-25 dB). These curves are quite different from both the previous ones and the solid red ones that were obtained with 45 loaded elements (about 15 m from the center, red solid circle in Fig. 5, $\left|\boldsymbol{a}^{(c)}/a_0\right|$>-35 dB). The slow convergence of the series is not surprising in view of the high excitation levels $\boldsymbol{a}^{(c)}/a_0$ shown in Fig. 6. The Z_{L}EEP in Fig. 7 exhibits very deep nulls in both *E*- and *H*-planes at about 10-20° from zenith. At this observation angle, the linear combination of the surrounding-element Z_0EEPs in (4) exhibits opposite phase with respect to the central-element Z_0EEP. It should be also noted that the loading of elements 1-15 (the denser quasi-regular central region) provides a Z_{L}EEP (dash-dotted magenta curve) which is quite close to the red curve (45 elements). This means that the effect of the outer elements, which are more randomly distributed, is smaller but still not negligible.

The parametrical analysis in Fig. 8 has been performed in order to show the high sensitivity of the Z_{L}EEP *E*-plane with respect to the amplifier reflection coefficient phase $\angle\Gamma_L$. A very deep null is present at zenith for $\angle\Gamma_L$ values around 323°.

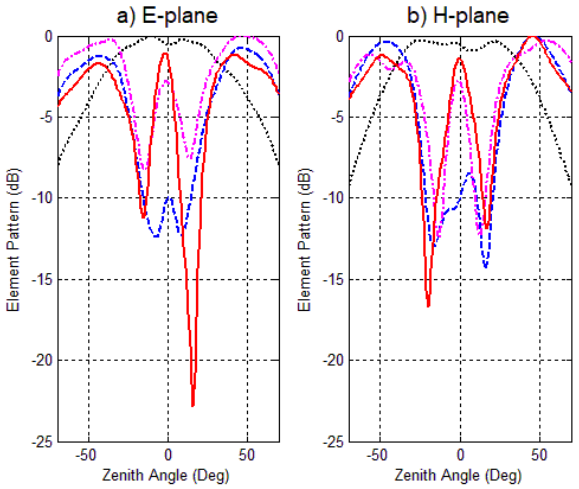

Fig. 7. Z_LEEP principal cuts for the LBA central element at 57 MHz, computed by loading an increasing number of adjacent elements (4): 0 (i.e. Z_0EEP, dotted black curves), 6 (dashed blue curve), 15 (magenta dash-dotted curve) and 45 (solid red curve)

Two asymmetrical nulls at about 10-20° from zenith (as in Fig. 7) are instead visible for $\angle\Gamma_L$ values ranging from 330° to 340°, which are consistent with the measured amplifier data reported in Fig. 4b). The nulls disappear below $\angle\Gamma_L$ =315° and above $\angle\Gamma_L$ =345°. The effect of $|\Gamma_L|$ (not shown) will instead mainly affect the null depth.

III. Experimental Validation

The experimental validation of such large low-frequency telescopes can only be performed in situ. Astronomical calibration sources [6],[19] or satellites have already been used to characterize both the sensitivity and radiation patterns at array levels i.e. after beam forming. Artificial sources mounted on micro-UAVs or cranes instead provide enough power and spatial coverage to allow for a full characterization at element level [18],[20]-[23]. In particular, the UAV solution shown in Fig. 3 allows for an even more complete spatial coverage than the crane, at a lower cost. It is based on a hexacopter frame carrying a 2-m long dipole. The dipole is fed from a multi-tone radio-frequency transmitter. The position and orientation of the test source in the sky are measured by the onboard Differential Global Navigation System (DGNSS) and the Inertial Measurement Unit, respectively. The hexacopter was programmed to perform constant-height linear trajectories corresponding to the principal planes of the LBA dipoles, which are oriented at 45° with respect to Cartesian reference system used in Fig. 5. The flight height was about 300 m in order to approach the far-field condition for the elements inside a 30 m diameter at 57 MHz. The received signals were directly acquired from the LOFAR back-end. The post-processing procedure in [24] was adopted to correct for both the source radiation pattern and the path loss.

The measured results for the LBA central element (#0) at 57 MHz (blue solid line with markers) are compared to simulations (section II.B) in Fig. 9 (solid red line). The overall

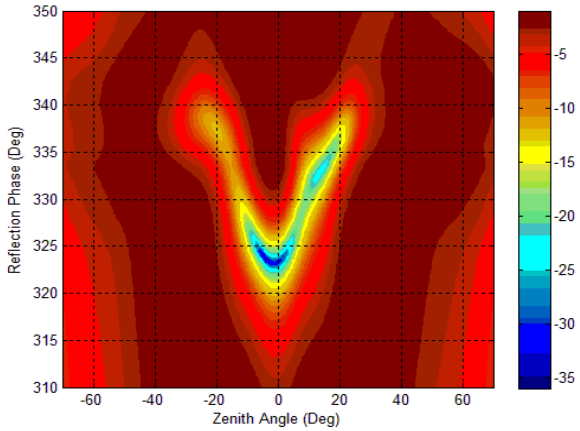

Fig. 8. *E*-plane pattern cuts (dB) of the LBA central element Z_LEEP at 57 MHz for different values of the amplifier reflection coefficient phase $\angle\Gamma_L$.

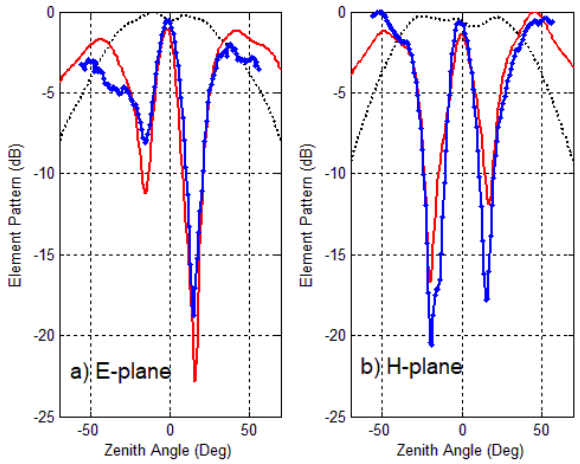

Fig. 9. Z_LEEP principal cuts for the LBA central element (#0) at 57 MHz: simulated (solid red line) and measured (blue line with markers). The Z_0EEP is reported with the dotted black line.

agreement can be considered as very good in view of the sensitivity analysis reported in Fig. 8 and the overall complexity of both the system under test and the measurement setup. The same consistency has been achieved for all other elements and for both polarizations. For example, Fig. 10 shows the *E*-plane patterns of elements #2 and #3 that are still close to the center. Their distorted behavior with respect to the Z_0EEP (dotted black line) is clearly visible in both measured and predicted data. As written in section II.B, the LBA elements that are further from the center also present a larger relative spacing and a more randomized distribution i.e. lower mutual coupling effects. Hence, the pattern distortion effect for those elements is less severe. However, the reported results for elements #26 and #42 in Fig.11 still show a significant discrepancy between the Z_LEEP and the corresponding Z_0EEP.

Finally, Fig. 12 shows the behavior of the central element at 44.5 MHz. As expected from the data in Fig. 4, the antenna-amplifier system is far from the resonance condition, therefore, the effect of the amplifier input impedance on the Z_LEEP is definitely smaller than at 57 MHz (see Fig. 9).

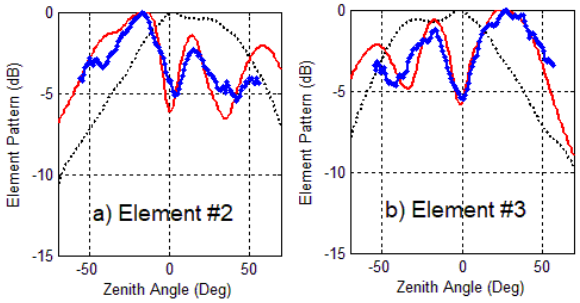

Fig. 10. Z_LEEP *E*-plane cuts at 57 MHz for LBA elements #2 and #3 (close to the center): simulated (solid red line) and measured (blue line with markers). The Z_0EEP is shown with the dotted black line.

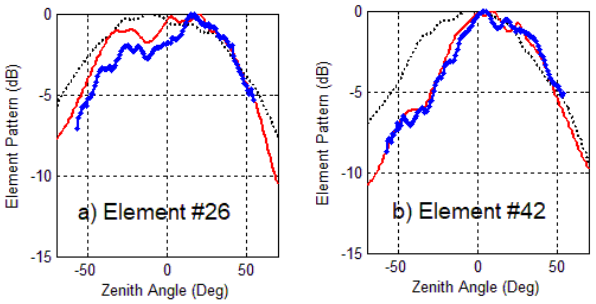

Fig. 11. Z_LEEP *E*-plane cuts at 57 MHz for LBA elements #26 and #42: simulated (solid red line) and measured (blue line with markers). The Z_0EEP is shown with the dotted black line.

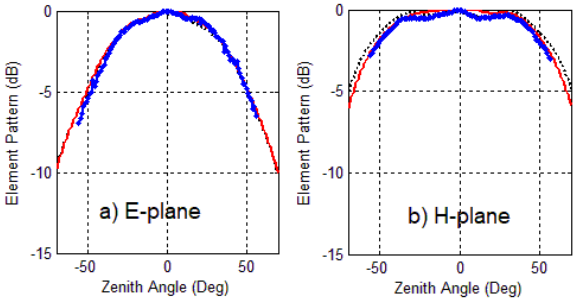

Fig. 12. Z_LEEP principal cuts for the LBA central element (#0) at 44.5 MHz: simulated (solid red line) and measured (blue line with markers). The Z_0EEP is shown with the dotted black line.

IV. Conclusion

The problem of sharp features in the EEPs of low-frequency receiving arrays has been thoroughly investigated with both models and experiment. The usage of narrow-band elements with sharp frequency behavior in conjunction with amplifiers with reactive impedances produces element patterns that are not smooth. The EEPs of the LOFAR LBA central elements exhibit nulls (Fig. 9) or quite deep minima (Fig. 10) within the field-of-view of the telescope. Elements that are further from the center still show significant ripple (Fig. 11) that can be demanding from the modeling point of view. This is a problem in terms of both telescope performance on a given frequency band and its characterization/calibration.

It has been demonstrated that the larger pattern distortion phenomena occur at the resonance frequency of the antenna-amplifier assembly i.e. the same frequency at which maximum telescope sensitivity is expected. This highlights an important criticality that should be controlled during any further telescope design work.

In random spare arrays, the sensitivity is proportional to the number of elements N. Therefore, each element null will provide a relative sensitivity reduction towards the corresponding observation angle of about $1/N$. It has been observed that the nulls/minima for the seven central elements do not occur at the same observation angle (see Fig. 9 and 10), therefore, such a degradation effect is distributed across the field-of-view. Within the LBA inner (46 elements), the maximum sensitivity reduction can hence be quantified as 2%.

Moreover, it has been found that the station calibration is often unsuccessful for those seven central elements. In this case, the required amplitude and phase correction are not applied to the final beamforming stage. According to a random-walk model, the uncalibrated seven central elements will only contribute with a factor of $\sqrt{7}$ (instead of 7) to the overall sensitivity. The corresponding sensitivity degradation can then be estimated in the order of 9%.

The presented activity led to a validated EM model that can be used to predict the station response for a given choice of beamforming weights. Such an accurate forward model of the station response will significantly reduce the direction-dependent errors after station gain and delay calibration, which in turn will reduce the computational burden in the imaging stage as fewer additional direction-dependent corrections are required. The availability of such models is therefore expected to be a valuable asset for imaging pipelines for phased array telescopes like LOFAR and SKA.

Acknowledgment

The authors thank Menno Norden and Michel Arts from ASTRON, Paolo Maschio, Irene Aicardi and Horea Bendea from Politecnico di Torino (DIATI), and Augusto Olivieri from CNR-IEIIT for their valuable technical contribution to the experimental activity.

References

[1] M. P. van Haarlem et al., "LOFAR: The LOw-Frequency Array", *Astronomy & Astrophysics*, vol. 556, **A2**, 1-53, Aug. 2013.

[2] S. J. Tingay et al., "The Murchison Widefield Array: The Square Kilometre Array Precursor at Low Radio Frequencies", Publications of the Astronomical Society of Australia, vol. 30, **7**, Jan. 2013

[3] P. E. Dewdney, P. J. Hall, R. T. Schilizzi and T. J. L. W.Lazio, "The Square Kilometre Array", *Proceedings of the IEEE*, vol. 97, **8**, 1482-1496, Aug. 2009

[4] S. J. Wijnholds, S. van der Tol, R. Nijboer, and A. J. van der Veen, "Calibration challenges for future radio telescopes," *IEEE Signal Processing Magazine*, vol. 27, **1**, 30-42, January 2010.

[5] S. Salvini, and S. J. Wijnholds, "Fast gain calibration in radio astronomy using alternating direction implicit methods: Analysis and applications," *Astronomy & Astrophysics*, vol. 571, **A97**, 1-14, November 2014.

[6] S. J. Wijnholds, and W. A. van Cappellen, "In Situ Antenna Performance Evaluation of the LOFAR Phased Array Radio Telescope," *IEEE Transactions on Antennas and Propagation*, vol. 59, **6**, 1981-1989, June 2011.

[7] IEEE Standard for Definitions of Terms for Antennas, IEEE Standard 145, 2013, pag. 14, definition of "embedded element pattern", NOTE 1.

[8] http://www.altairhyperworks.com/product/FEKO

[9] F. Farzami, S. Khaledian, B. Smida and D. Erricolo "Pattern-Reconfigurable Printed Dipole Antenna Using Loaded Parasitic Elements", *IEEE Antennas and Wireless Propagation Letters*, vol. 16, 1151-1154, 2017

[10] R. F. Harrington, "Reactively Controlled Directive Arrays," *IEEE Transactions on Antennas and Propagation*, vol. AP-26, 3, 390-395, May 1978.

[11] M. Beruete, I. Campillo, J. S. Dolado, J. E. Rodríguez-Seco, E. Perea, F. Falcone, and M. Sorolla, "Very Low-Profile "Bull's Eye" Feeder Antenna", IEEE Antennas and Wireless Propagation Letters, vol. 4, 365-368, 2005.

[12] A. Neto, N. Llombart, G.Gerini, and P. De Maagt, "On the Optimal Radiation Bandwidth of Printed Slot Antennas Surrounded by EBGs", IEEE Transactions on Antennas and Propagation, vol. 54, 4, 1074-1083, April 2006.

[13] M. Ettorre, S. Bruni, G. Gerini, A. Neto, N. Llombart, and S. Maci, "Sector PCS-EBG Antenna for Low-Cost High-Directivity Applications", IEEE Antennas and Wireless Propagation Letters, vol. 6, 537-539, 2007.

[14] A. Sutinjo, M. Okoniewski, and R. H. Johnston, "A Holographic Antenna Approach for Surface Wave Control in Microstrip Antenna Applications", IEEE Transactions on Antennas and Propagation, vol. 58, 3, 675-682, March 2010.

[15] H. A. Haus and R. B. Adler, "Circuit Theory of Linear Noisy Networks", MIT and John Wiley and Sons, 1959

[16] P. Bolli, et al., "Antenna pattern characterization of the low-frequency receptor of LOFAR by means of an UAV-mounted artificial test source," in *Proceedings SPIE - Ground-based and Airborne Telescopes VI*, vol. 9906, July 2016.

[17] D. Gonzalez-Ovejero, E. de Lera Acedo, et al., "Non-periodic arrays for radio-astronomy applications," *IEEE International Symposium on Antennas and Propagation and USNC/URSI National Radio Science Meeting*, Spokane, 2011,pp. 1762 - 1765

[18] A. Nelles, et al, "Calibrating the absolute amplitude scale for air showers measured at LOFAR", JINST 10 (2015) no.11, P11005 arXiv:1507.08932

[19] A. T. Sutinjo, et al. "Characterization of a Low-Frequency Radio Astronomy Prototype Array in Western Australia", *IEEE Trans. on Antennas Propag.*, Vol. 63, **12**, December, 2015

[20] G.Virone, et al, "Antenna pattern verification system based on a micro unmanned aerial vehicle (UAV)", *IEEE Antennas and Wireless Propagation Letters*, vol. 13, 169-172, Jan. 2013.

[21] G. Pupillo, et al., "Medicina Array Demonstrator: Calibration and Radiation Pattern Characterization Using a UAV-Mounted Radio-Frequency Source", *Experimental Astronomy*, vol. 39, **2**, 405-421, Jun. 2015.

[22] E. de Lera Acedo, et al., 'SKA Aperture Array Verification System: Electromagnetic modeling and beam pattern measurements using a micro UAV', accepted for publication in *Experimental Astronomy*

[23] P. Bolli, S. J. Wijnholds, E. de Lera Acedo, A. Lingua, J. Monari, F. Paonessa, G. Pupillo, G. Virone, "In-Situ Characterization of International Low-Frequency Aperture Arrays by Means of an UAV-based System", on *32nd URSI GASS*, Montreal, 19-26 August 2017

[24] G. Virone, et al., "Antenna pattern measurements with a flying far-field source (hexacopter)," in IEEE International Conference on Antenna Measurements and Applications (CAMA), Antibes Juan-les-Pins, France, Nov. 16-19 2014.